Correction of CT artifacts and its influence on Monte Carlo dose calculations

Magdalena Bazalova
Medical Physics Department, McGill University, Montreal General Hospital, 1650 Cedar Avenue, Montreal, Québec, H3G1A4, Canada

Luc Beaulieu
Département de Physique, de Génie Physique et d'Optique, Université Laval, Québec City, Québec, Canada G1K7P4 and Département de Radio-Oncologie, Hôtel Dieu de Québec, Centre Hospitalier Universitaire de Québec, Québec City, Québec, Canada G1R2J6

Steven Palefsky and Frank Verhaegen[a)]
Medical Physics Department, McGill University, Montreal General Hospital, 1650 Cedar Avenue, Montreal, Québec, H3G1A4, Canada

(Received 26 September 2006; revised 3 April 2007; accepted for publication 4 April 2007; published 21 May 2007)

Computed tomography (CT) images of patients having metallic implants or dental fillings exhibit severe streaking artifacts. These artifacts may disallow tumor and organ delineation and compromise dose calculation outcomes in radiotherapy. We used a sinogram interpolation metal streaking artifact correction algorithm on several phantoms of exact-known compositions and on a prostate patient with two hip prostheses. We compared original CT images and artifact-corrected images of both. To evaluate the effect of the artifact correction on dose calculations, we performed Monte Carlo dose calculation in the EGSnrc/DOSXYZnrc code. For the phantoms, we performed calculations in the exact geometry, in the original CT geometry and in the artifact-corrected geometry for photon and electron beams. The maximum errors in 6 MV photon beam dose calculation were found to exceed 25% in original CT images when the standard DOSXYZnrc/CTCREATE calibration is used but less than 2% in artifact-corrected images when an extended calibration is used. The extended calibration includes an extra calibration point for a metal. The patient dose volume histograms of a hypothetical target irradiated by five 18 MV photon beams in a hypothetical treatment differ significantly in the original CT geometry and in the artifact-corrected geometry. This was found to be mostly due to miss-assignment of tissue voxels to air due to metal artifacts. We also developed a simple Monte Carlo model for a CT scanner and we simulated the contribution of scatter and beam hardening to metal streaking artifacts. We found that whereas beam hardening has a minor effect on metal artifacts, scatter is an important cause of these artifacts. [DOI: 10.1118/1.2736777]

Key words: CT scanner, CT metal artifacts, HU calibration, Monte Carlo calculation

I. INTRODUCTION

The aim of cancer radiotherapy is to deliver a prescribed radiation dose to a defined tumor volume while minimizing the damage to the surrounding healthy tissue. An important step in cancer radiotherapy is the treatment planning. It is frequently done on the basis of CT (Computed tomography) images. CT images are represented by Hounsfield units, defined as $HU=1000(\mu/\mu_w-1)$, where μ and μ_w are the linear attentuation coefficients of a material and water, respectively. During the planning, the tumor and organs at risk are delineated and the dose to these structures and to normal tissue is determined. The treatment plan is then optimized until all dose requirements usually set by a physician are met.

Two approaches to calculate the dose delivered to patients are currently in use. Whereas in conventional treatment planning the dose is calculated using a model in which patients consist of water (possibly considering electron density), in Monte Carlo treatment planning (MCTP), the CT image is segmented into a few materials (e.g., air, tissue, bone), and the dose is calculated taking these media into account. In the ideal case, the MCTP leads to more accurate dose calculation.[1] However, due to potential artifacts in CT images, inaccuracies in assigning of HU might result in significant dose miscalculation in both treatment planning methods. Due to an additional miss-assignment of media in MCTP, this method can potentially lead to larger dose calculation errors than conventional treatment planning, which is the research topic of this paper.

The origins of CT artifacts, discrepancies between reconstructed HU in CT images and the true attenuation coefficients, are believed to be known.[2] Metal streaking artifacts appear when a high atomic number, high density material is present in a scanned object which might severely degrade image quality. For example, in between two hip prostheses in a patient's body there is practically no information about the patient's geometry which can be detrimental for treatment planning. Bright and dark streaks not only disallow tumor and organ delineation but might also cause dose miscalcula-

tion. As a result, there is a strong need to reduce CT artifacts in MCTP due to potential incorrect assignment of media. The purpose of this work is to investigate the effect of metal streaking artifact correction on CT image quality and Monte Carlo (MC) dose calculations.

Streaking artifact correction algorithms have been developing in recent years. The simplest approach that can be used for minor artifacts is to correct for discrepancies in the CT images themselves.[3] The more sophisticated approaches use three main techniques: filtered back-projection (FBP) on a modified sinogram,[4–6] filtering techniques,[7] and iterative algorithms.[8–12]

Filtered back-projection on a modified sinogram artificially fills corrupted segments in sinograms that correspond to projections containing high density materials. Kalender, Hebel, and Ebersberger[4] used linear interpolation within each projection, while Roeske *et al.*[5] applied a cubic spline fit to correct for artifacts in images containing Fletcher-Suit applicator. Yazdi, Gingras, and Beaulieu[6] in their recent work also used neighboring projections at different angles to correct for metal artifacts in CT images of patients with hip prostheses.

Iterative algorithms can use different techniques, such as iterative deblurring[8–11] and the maximum likelihood algorithm.[12] Although iterative algorithms usually result in slightly better image quality, they need longer computation time which makes them currently impractical for clinical use.

In this paper, a FBP method on modified raw data is demonstrated that uses cubic interpolation of missing sinogram data. The correction algorithm is used on various cylindrical phantoms and on a prostate patient. The impact of the correction method on Monte Carlo dose calculation for both phantoms and the patient is determined. Moreover, scatter and beam hardening are briefly studied as potential causes to metal streaking artifacts.

II. MATERIALS AND METHODS

A. Scanning protocols and phantoms

A fourth generation single slice Picker PQ5000 CT scanner was used to acquire images of two cylindrical water phantoms (15 and 27 cm in diameter) simulating head and pelvis anatomies. The phantoms were scanned in axial mode at 120 kVp and 400 mAs. Both full field and half field sizes of the scanner were used, resulting in 512×512 pixel images. The HU range in the original CT image from the scanner is $[-1000, 3095]$.

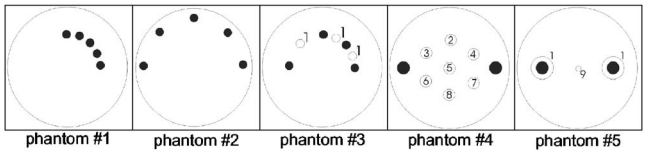

FIG. 1. Schematic overview of three cylindrical head phantoms (1, 2, and 3, 15 cm in diameter) with small steel cylinders (1.3 cm in diameter) mimicking dental fillings and of two cylindrical pelvic phantoms (4 and 5, 27 cm in diameter) with large steel cylinders (2.8 cm in diameter) mimicking hip prostheses. The full circles represent steel cylinders, the remaining materials are listed in Table I.

The two phantoms were scanned with various inserts, holding steel cylinders mimicking dental fillings or hip prostheses, Teflon cylinders mimicking bone, and vials with different in-house made solutions of ethanol and calcium compounds. Steel was chosen as one of three commonly used hip prosthesis materials.[13] In this paper, artifact correction results of five phantoms are presented: phantoms 1, 2 and 3 are head phantoms; phantoms 4 and 5 are pelvic phantoms (Fig. 1). Phantoms 1 and 2 are similar phantoms that contain five small steel cylinders to simulate dental fillings positioned either close together or further apart. The small cylinders are placed closer to the phantom surface in phantom 2, so that electron MC dose calculation can be done. Phantom 3 consists of four steel cylinders interleaved by three small Teflon cylinders that mimic teeth.

Phantom 4 contains two large steel cylinders and seven vials filled with water solutions of ethanol C_2H_5OH, calcium chloride $CaCl_2$, calcium perchlorate $Ca(ClO_4)_2$, and calcium nitrate $Ca(NO_3)_2$ with densities varying from 0.838 to 1.184 g/cm^3 (Table I).

Phantom 5 consists of two steel cylinders embedded in Teflon cylinders to simulate hip prostheses surrounded by bone. A $Ca(ClO_4)_2$ water solution with density of 1.692 g/cm^3 is placed in the center of the phantom.

In the case of the prostate patient, a helical sinogram consisting of 66 slices was processed and the artifact correction

TABLE I. Composition by fractional weight of Teflon cylinders and solutions used in the phantoms.

			Fraction by weight						
No.	Material/solution	ρ (g/cm^3)	H	C	N	O	F	Cl	Ca
1	Teflon	2.200		24.02			75.98		
2	$Ca(NO_3)_2$	1.045	10.41		1.19	86.69			1.71
3	C_2H_5OH	0.931	11.93	19.81		68.26			
4	$CaCl_2$	1.184	8.29			65.78		16.56	9.37
5	C_2H_5OH	0.838	12.66	39.63		47.71			
6	$Ca(ClO_4)_2$	1.119	9.33			82.93		4.94	2.80
7	$CaCl_2$	1.025	10.66			84.58		3.04	1.72
8	C_2H_5OH	0.883	12.30	29.72		57.98			
9	$Ca(ClO_4)_2$	1.692	3.88			65.77		19.39	10.96

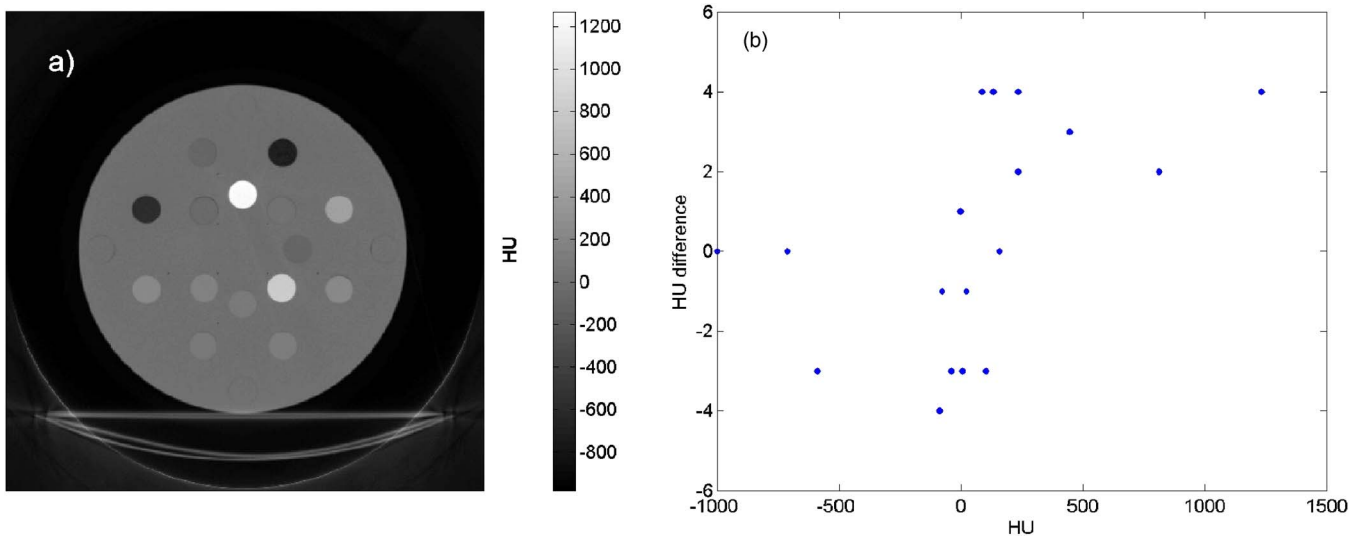

FIG. 2. The RMI electron density calibration phantom (a) and the differences between the mean HU as reconstructed by the CT scanner and by our algorithm for 18 materials.

algorithm was applied on 672×672 pixel images. The patient's hip prostheses extended from slice 30 to slice 66.

We developed an algorithm that converts raw data from the scanner into images. To ensure that the procedure works well and reconstructs correct HU, an RMI electron density calibration phantom [Fig. 2(a)] was used to test it. The mean HU of 18 materials obtained directly from the scanner and reconstructed by the procedure were compared, the absolute differences for each material are plotted in Fig. 2(b). The tested HU range extends from −1000 to 1250. The HU were reconstructed accurately within ±4 HU with our procedure.

B. Artifact correction algorithm

The artifact reduction algorithm used in this work is based on interpolation of raw sinogram data. The basic steps are identification of the projections corresponding to metals and their interpolation in sinogram space. As a result, the interpolated sinogram is used to obtain an artifact-corrected image. We have developed a MATLAB routine to which a fan beam sinogram is the input and an artifact-corrected image is the output.

First, sinograms from a CT scanner are extracted and transferred to a PC where the correction algorithm is performed. The fan beam sinograms are converted into parallel beam sinograms using Fourier analysis.[14] The correction algorithm itself (Fig. 3) is based on work by Roeske *et al.*[5] and Yazdi, Gingras, and Beaulieu[6] and starts by identifying projections corresponding to high density voxels. For this purpose, filtered back-projection of the parallel beam sinogram is performed resulting in an original image containing artifacts produced by metals. The HU scale of the original image reconstructed from the sinogram is unlimited as opposed to the original image from the CT scanner with the maximum HU of 3095. The voxels corresponding to metals are detected by a fixed threshold in the original image. The threshold has been tested on various geometries and it has been established to be 3800 HU for our scanning protocol. A new image of only high density voxels—a metal only image—is produced. Its forward Radon transform defines a mask for the original sinogram and consequently the missing projections over which an interpolation has to be applied. The masked sinogram in which the interpolation is performed is created by applying the mask to the original sinogram. The cubic spline interpolation is done at each projection angle of the masked sinogram as follows. First, the missing projections are found. To make sure interpolated data will be consistent, two neighboring projection values of the same projection angle on both sides of the missing projections are taken into account. The cubic spline fit is performed on the basis of the four neighboring projections at every projection angle and hence the interpolated sinogram is created. FBP of the modified sinogram produces an artifact-corrected image not containing metals, because their projections have been replaced by the interpolation. The final artifact-corrected image is created by superposition of the metal-only image on the corrected image without metals.

C. MC dose calculation and extended calibration

The influence of the metal artifact reduction method on MC dose calculation was examined with the EGSnrc/DOSXYZnrc code[15] in a set of beam geometries. The original and corrected images were converted into mass densities and segmented into materials according to the standard DOSXYZnrc/CTCREATE calibration which uses four materials: air, lung, tissue, and bone. It is common practice to use four materials for MC dose calculation. Several authors use the exact CTCREATE ramp with the default HU and density limits,[16,17] while others[1,18–20] keep the four media and slightly modify the HU and density limits. Some authors segment CT images into less than four materials for MC dose calculations.[21–24] Du Plessis *et al.*[25] segment CT images into seven materials and Schneider, Bortfeld, and Schlegel[26] into

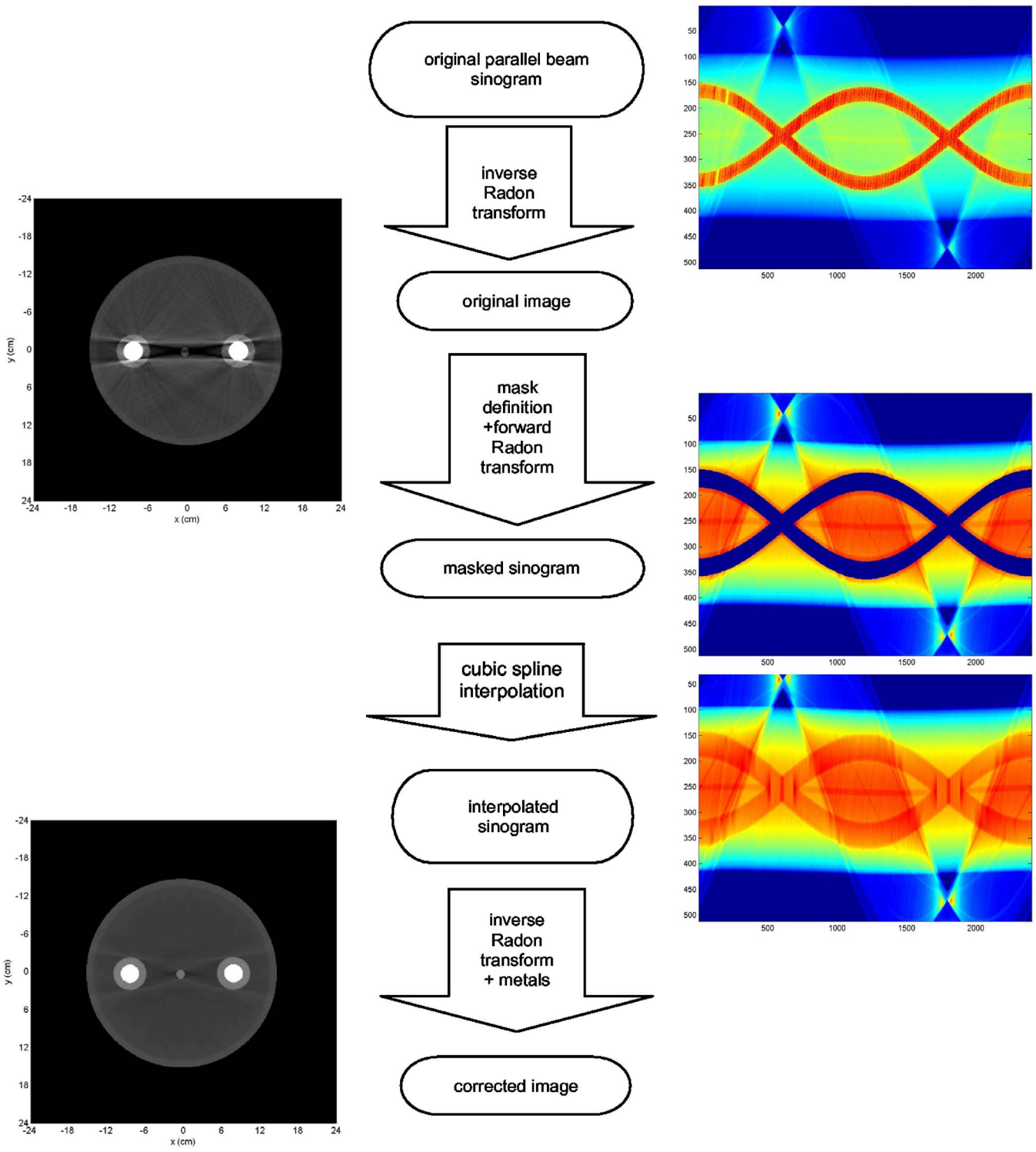

FIG. 3. Flow chart of metal artifact correction algorithm.

71 materials for MC dose calculations, however, this approach is rare. In our work, we have used the HU and density limits given by the DOSXYZnrc/CTCREATE ramp. Since we knew there was no lung in the phantoms or the patient, the lung calibration point was excluded from our conversion.

We have noticed an important issue in our Monte Carlo simulations using the CTCREATE calibration. It was found that in the presence of foreign metal objects, an extra calibration point for a metal must be added to the standard DOSXYZnrc calibration in order to obtain agreement between exact geometry MC dose calculations and dose calculations based on CT image geometry. The limited HU scale[27] of our CT scanner with a maximum value of 3095 together with the present calibration makes it impossible to retrieve densities higher

TABLE II. HU and mass density (ρ) intervals used for conversion of HU into densities and materials for MC dose calculations. Steel is the added calibration point compared to the standard DOSXYZnrc calibration.

Material	HU interval	ρ interval
Air	[−1000:−950]	[0.001: 0.044]
Water/tissue	[−950:125]	[0.044: 1.101]
ICRP cortical bone	[125: 2000]	[1.101: 2.088]
Steel	**3095**	**8.055**

than 2.664 g/cm^3. In comparison, the density of steel is 8.055 g/cm^3. Since there is no bone in the human body that has a HU of 3095 in the energy range of typical CT x-ray tubes, in our calibration, all voxels with 3095 HU are set to steel with density of 8.055 g/cm^3. We denote the calibration as an *extended calibration* (Table II). For phantom dose calculations, the second segment of the calibration curve corresponds to water, whereas in the patient study, ICRU tissue (International Commission on Radiation Units and Measurements) is used for the same HU interval.

In our work, we have found that omitting the extended calibration in the presence of metals leads to large dose calculation errors. All dose calculation results in this paper were obtained with the extended calibration, unless stated otherwise.

In phantoms, the dose was calculated in original and corrected CT images in a set of beam arrangements, 6 and 18 MV broad polyenergetic photon beams (four field box, two parallel opposed beams) and a single 18 MeV broad polyenergetic electron beam were used for dose calculations. The spectra were taken from Mohan, Chui, and Lidofsky.[28] The isocenter was placed in the center of the phantoms in all MC simulations. Since we acquired single slice images in our phantom study, we used the reciprocity theorem[29] to score dose in the phantoms. We created the three-dimensional phantoms by adding a 10 cm z dimension to the two-dimensional (2D) slices. In addition to that, we used 1-cm-thick beams perpendicular to the z axis to make sure all laterally scattered electrons were captured within the phantom. As a result, the voxel sizes for head phantom calculations were $(0.47\times0.47\times100)$ mm^3 and for pelvic phantoms $(0.94\times0.94\times100)$ mm^3 and all beams were then of 1 cm length in the z axis and of varying width in the perpendicular direction. The 6 MV photon beam used in the phantom 1 was 8 cm wide, the 18 MV photon beams were used in the pelvic phantoms and were 10 cm wide. The 8 cm 18 MeV electron beam was simulated at an angle of 315° in the phantom 2. The dose distributions were then compared to exact geometry dose calculations. To quantify the dose differences, a target has been delineated in all phantoms. Dose calculation results of phantoms 1, 4, and 5 are analyzed by the mean errors of a cylindrical target placed in the center of the phantom. The electron dose distributions in phantom 2 are compared by means of dose calculation errors in an ellipsoidal target.

For the prostate patient, a hypothetical five 18 MV photon beam (0°, 90°, 270°, 110°, and 250°) treatment was simulated in the DOSXYZnrc code. The photon beam size was 7×7 cm^2 and the isocenter was placed in the center of the prostate. The 90° and 270° beams were shot straight through the prostheses. It has to be noted that this technique is rather theoretical and treating straight through both prostheses should be avoided. Nevertheless, it is very difficult to avoid the prostheses totally with the five beam technique that is used in our hospital. A hypothetical target in the shape of an ellipsoid was delineated around the prostate. The target was 6 cm long with a semimajor and a semiminor axis of 3 and 2 cm, respectively, defining a volume of 50 cm^3. The voxel size for patient dose calculation was defined by the scan parameters to be $(0.744\times0.744\times4.25)$ mm^3. Although it was not known what the hip prostheses were made of, for the MC dose calculation the metallic material was set to steel for this hypothetical case. The results of the original CT geometry and the artifact-corrected geometry were compared by dose distributions and dose volume histograms (DVHs) of the target. Exact dose calculations for the patient were not possible.

All Monte Carlo dose calculations presented have statistical errors less than 0.5% in high dose regions.

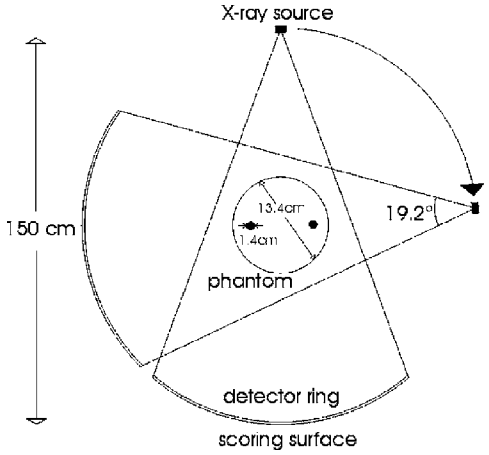

FIG. 4. Schematic view of the geometry for the scatter study. The full circles are steel cylinders.

D. MC simulation of sources of metal streaking artifacts

Although origins of artifacts are mostly known, discussion on causes of metal streaking artifacts is still an issue. De Man *et al.*[30] and Williamson *et al.*[31] using mathematical simulations show that beam hardening, scatter, and noise are the dominant causes of metal streaking artifacts. In this study, we used the Monte Carlo method to simulate a CT scanner and evaluated the effect of scatter and beam hardening on the metal streaking artifacts. We produced sinograms of a phantom by modifying the DOSXYZnrc code such that it is possible to track scattered particles and save them in a separate sinogram.

A schematic view of the simulation geometry is shown in Fig. 4. The phantom was a cylindrical phantom filled with water and containing two small steel cylinders. The source of

x rays in our simulation is a phase-space file created by the MC simulation of a CT scanner using the BEAMnrc code.[32] We used two types of x rays: a polyenergetic x-ray beam that is used in real CT scanners and a mono-energetic x-ray beam that can be used for evaluation of beam hardening on streaking artifacts. The polyenergetic spectrum was obtained by simulation of an x-ray tube with 120 keV electrons striking a tungsten target that was simulated according to manufacturer's specifications. The spectrum was validated by half value layer (HVL) measurements and spectral measurements taken with a high resolution Schottky CdTe detector (XR-100T, AMPTEK Inc, Bedford, MA). A simple model for our single slice Picker PQ5000 CT was developed by adding two collimators that shape the beam to a 19.6° fan beam with a width of 1 cm at the detector ring. Identical collimation was used for the monoenergetic x-ray beam.

The source of x rays rotated in 1° steps about the CT scanner isocenter which was placed in the center of the phantom. The x-ray source irradiated the phantom from 200 positions, because the minimal data set for image reconstruction in our fan beam geometry requires a 200° rotation.[33]

The detector ring consists of 128 $CdWO_4$ detectors. Their response to x rays in energy range of our interest was simulated in the DOSXYZnrc code by calculating the dose deposited in $(29\times4\times0.945)$ mm^3 $CdWO_4$ crystals. Put another way, when a photon trajectory intersects the detector ring, its energy is convolved with the energy response of the detector crystals and the resulting signal is stored in the corresponding detector. In this way, an intensity map is created consisting of 128 detector readings at 200 projection angles.

A sinogram is a 2D map of projections $p=-\ln(I/I_0)$, where I is the intensity at the detector ring in the presence of attenuating object and I_0 is the source intensity at the detector ring. The source intensity map is simulated with no phantom. Subsequently a 200° sinogram is obtained. The sinogram is then completed in MATLAB to a 360° sinogram, converted into a parallel beam sinogram[14] and reconstructed. In a CT scanner, the x rays pass through a patient towards the detector ring and the attenuated photons generate a signal for image reconstruction. The reconstruction process (FBP) assumes that the detector signal consists of only primary attenuated photons. However, this is not the case in real CT scanners. There is a certain amount of scattered photons that reach the detector and their signal is incorrectly taken into account in the FBP. The scattered photon signal is negligible when scanning low density objects but it plays an important role when a high density material is present in the scanned object. Since the attenuation of x rays in thick high density materials is excessive, the signal in the shadow of these materials consists almost entirely of the scattered photons. This is a part of the detector-model mismatch introduced by Williamson.[31]

In our MC simulations, it is possible to track all interactions the x rays undergo, including the scatter. All the scattered photons were tagged and two different sinograms have been produced: a primary sinogram of primary photons and a sinogram of the tagged scattered photons. The total sinogram that the real CT scanners use is obtained by their summation. The effect of scattered photons on metal streaking artifacts is studied by comparison of two images: the original image reconstructed from the total sinogram and the scatter-free image that is obtained by a FBP of the primary sinogram.

The reconstruction algorithm also assumes that each voxel is represented by a constant, the linear attenuation coefficient of the voxel material. However, low energy photons of a polyenergetic spectrum are attenuated more easily than the high energy photons, which results in a higher effective beam energy as the beam passes through material. Consequently, the attenuation in every voxel is dependent on the mean beam energy at its position, which makes it difficult to assign a single value of the linear attenuation coefficient to that voxel. To investigate the effect of beam hardening, we simulated an x-ray tube with a single energy so that the beam cannot get harder and a single attenuation value to each voxel can be assigned. We used the energy of 75 keV which is approximately the mean energy of a common 120 kVp CT spectra. In this setup, we produced and processed a total and a primary sinogram in order to study the scatter contribution as well.

III. RESULTS AND DISCUSSION

The results are presented in four sections. The first two sections contain phantom images and dose calculations in phantoms and the third part is dedicated to patient MC simulation. The fourth part summarizes the results on the effects of scatter and beam hardening on metal streaking artifacts.

A. Corrected images

The artifact correction algorithm was used on several cylindrical phantoms and their results are presented in Fig. 5. Comparison of the first and the second columns that contain original CT and artifact-corrected images clearly demonstrates an improvement in image quality. Phantoms 1 and 2 are head phantoms with artifacts produced by steel cylinders that mimic tooth fillings. Phantom 3 also contains three small Teflon cylinders that are placed between fillings and are poorly visible in the original image. The correction algorithm cleans up the large artifacts and the Teflon cylinders can be distinguished. The pelvic phantoms (4 and 5) are more complex with major artifacts that severely influence the image. The original CT image of phantom 4 does not display the central vial with density of 0.838 g/cm^3. However, the vial is completely visible in the artifact-corrected image. Phantom 5 demonstrates the ability of the algorithm to distinguish between bone (Teflon) and metal; it validates the metal threshold choice. Due to artifacts, more voxels than just the steel cylinders have the maximum HU (3095) in the original image acquired by the CT scanner which makes it impossible to detect high density voxels directly in the original image by setting the threshold to 3095 HU. Nevertheless, after the original sinogram is processed, an unlimited HU scale can be used and a suitable threshold larger than the maximum HU in the CT images for metal detection of the artifact correction algorithm can be found. We have investigated the threshold

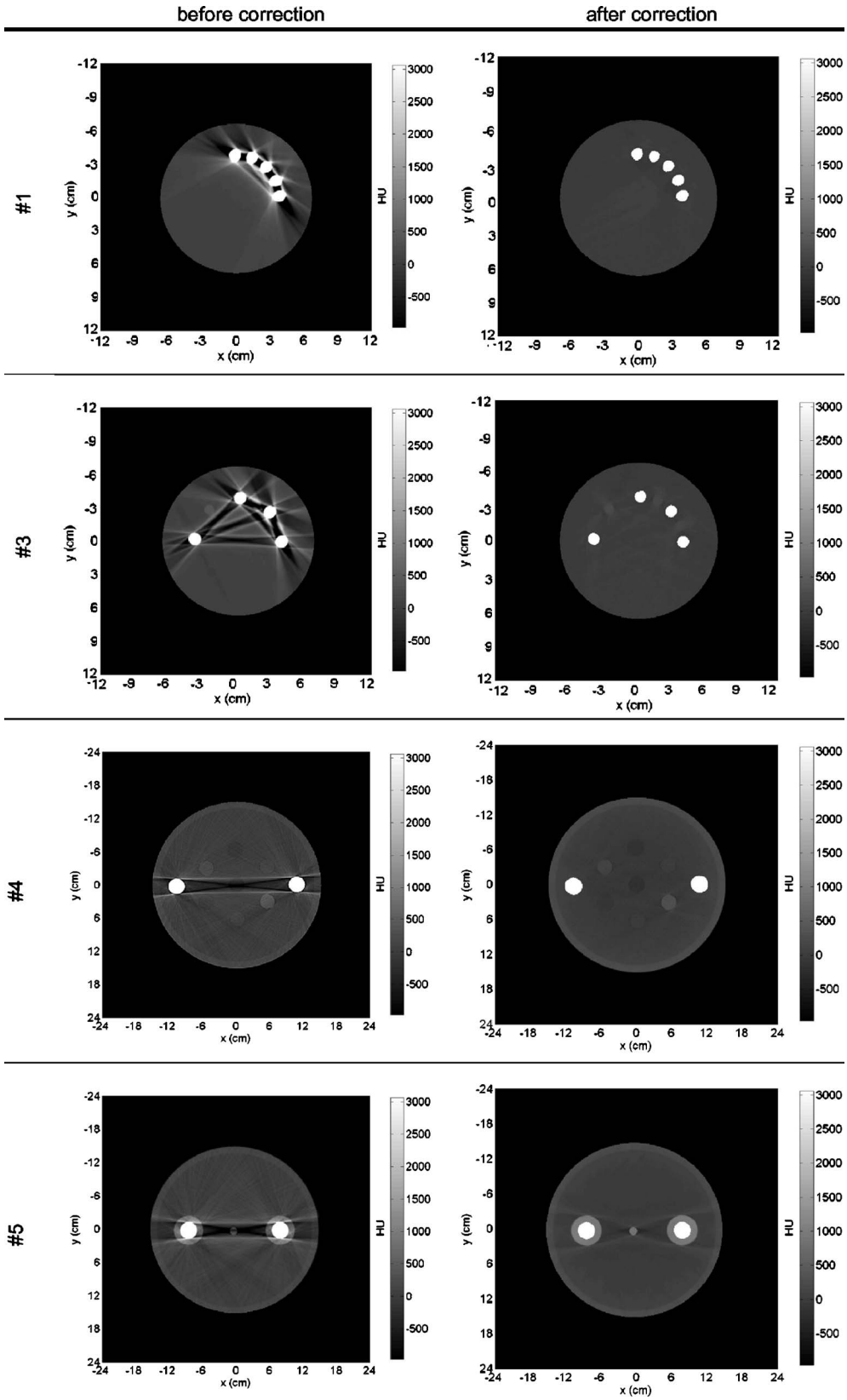

FIG. 5. Original images (first column) and artifact corrected CT images (second column) for phantoms 1, 3, 4, and 5. Phantom is 2 not shown, the results are similar to phantom 1.

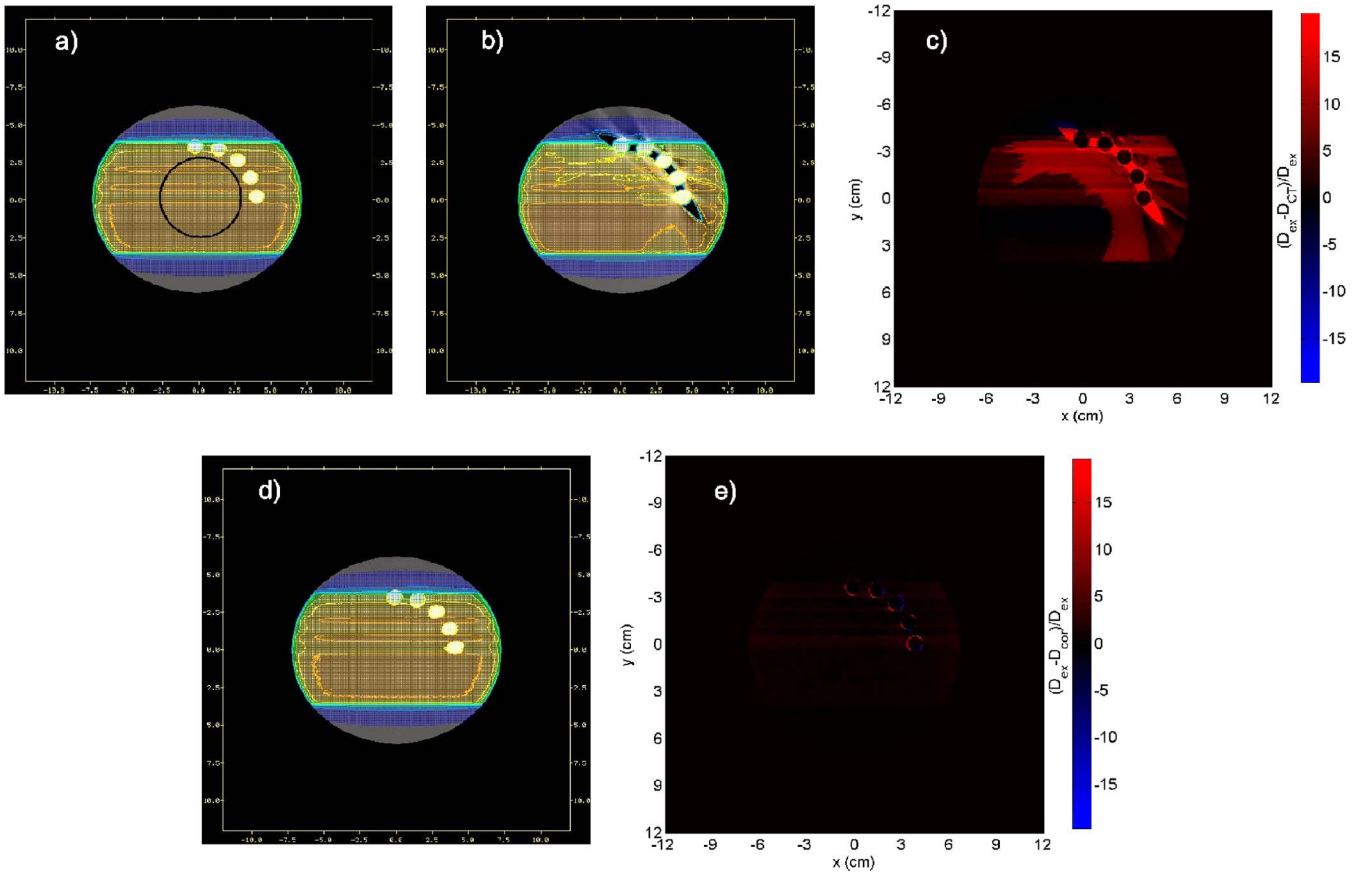

FIG. 6. Monte Carlo dose calculation in phantom 1 for two parallel opposed 6 MV photon beams. Exact geometry dose distribution D_{ex} with a hypothetical target outlined in black (a), original CT-based geometry D_{CT} (b) and artifact corrected geometry D_{cor} (d) dose distributions both with use of the extended calibration. The corresponding dose distribution differences from the exact geometry are presented in (c, e).

on various phantoms and we have established it to the value of 3800 HU. The corrected image of phantom 5 shows that the threshold used in the artifact correction algorithm for metal detection can distinguish between higher density materials, such as Teflon, and metal. It should be pointed out that the choice of Teflon as bone equivalent material is not suitable.[34] The presence of fluorine in Teflon gives low HUs compared to bone for the same mass density. Consequently, our calibration curve based on real human tissues is not able to retrieve the density of Teflon (2.2 g/cm^3) from its relatively low HU (400).

B. Phantom Monte Carlo dose calculation

The importance of the metal streaking artifact correction algorithm for MCTP is demonstrated by a set of MC dose calculations. We performed dose calculations in the exact phantom geometry (D_{ex}), in original CT geometry (D_{CT}), and in artifact-corrected CT geometry (D_{cor}). In Figs. 6–8, the dose differences $(D_{ex}-D_{CT})/D_{ex}$ and $(D_{ex}-D_{cor})/D_{ex}$ for 6 MV photon beams, an 18 MeV electron beam and 18 MV photon beams are displayed. Hypothetical targets have been delineated in individual dose distributions and their mean and maximum dose calculation errors are summarized in Table III.

To illustrate the need for the extended calibration, differences in MC dose distributions for two parallel opposed 6 MV beams where evaluated when the extended calibration for HU conversion *was not used* (results not shown). The significance of the extended calibration can be clarified by comparison of dose calculation errors in the artifact-corrected geometry. Whereas the mean error of the calculation in the target with the standard calibration is 2.6%, it decreases to 0.7% when the extended calibration is used [Fig. 6(e)]. To emphasize the influence of the extended calibration, one should note that the maximum error of the target in the artifact-corrected geometry with the extended calibration is only 1.9%, whereas without the extended calibration it is 7.7%. The mean and maximum error of the target in the original geometry [Fig. 6(c)] is 4.6% and 13.6%, respectively.

An important conclusion can be drawn from the presented 6 MV photon dose calculations. The maximum dose calculation errors decreased significantly from more than 25% in the original image without using the extended calibration to less then 2% in the artifact-corrected image with the extended calibration. In other words, only the combination of the artifact correction and the use of the extended calibration provides good dose calculation results. Clearly, the CTCREATE defaults should not be used for treating with metal im-

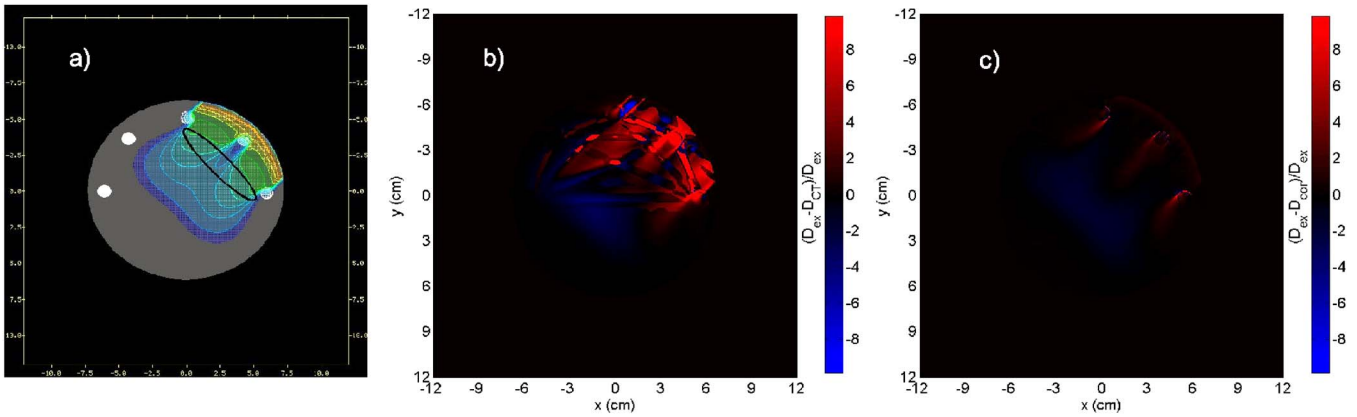

FIG. 7. An 18 MeV electron beam dose distribution in a head phantom (phantom 2). Exact geometry (a) and dose calculation errors in original CT (b) and in artifact-corrected (c) geometry.

plants. In the rest of the work, only the extended calibration for material and density conversion will be used.

For the purpose of the single 18 MeV electron beam dose calculation, phantom 2 has been constructed with steel cylinders close to its surface (Fig. 7). The mean dose errors in the hypothetical ellipsoidal target decreased significantly from 4.3% in the original CT image to 0.4% in the artifact-corrected image. Two photon beam dose calculations were performed with an 18 MV photon beam on two pelvic phantoms, phantom 4 and phantom 5 (Fig. 8). For phantom 4, a four field box beam arrangement was chosen. The mean dose differences in the target improved significantly from 3.1% in the original CT geometry to 0.6% in the artifact-corrected geometry.

Phantom 5 containing steel cylinders embedded in Teflon was simulated with two parallel opposed beams. Since there are large differences in mass energy absorption coefficients between Teflon and cortical bone (about 10% for a 6 MeV photon), in this case, we used a special approach for material and mass density assignment. We did not want to introduce

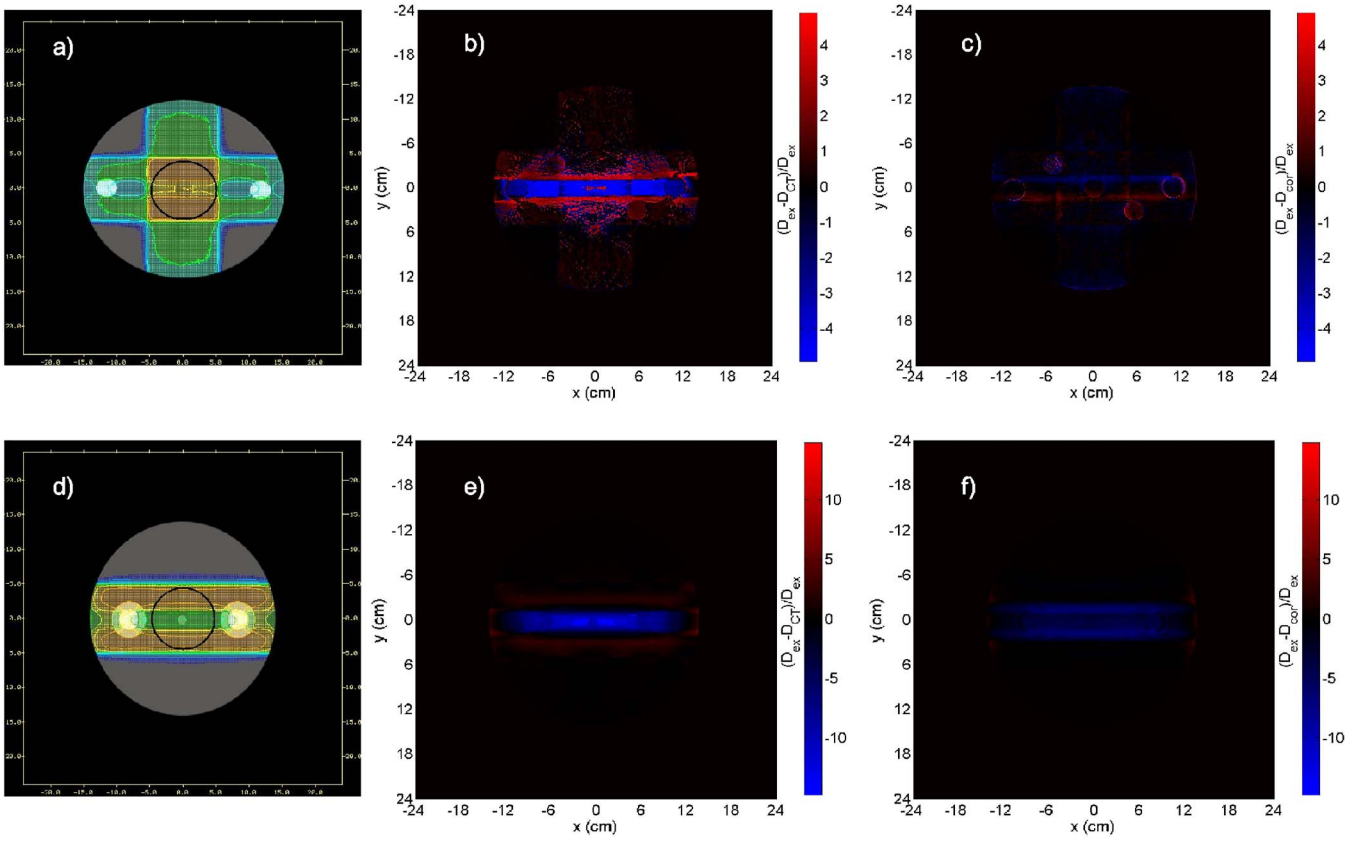

FIG. 8. An 18 MV photon beam dose distributions for two pelvic phantoms: phantom 4 (top) and phantom 5 (bottom). Exact geometry dose distribution (a, d), and differences from it in original CT image (b, e) and in metal artifact-corrected image (c, f).

TABLE III. Percentage mean and maximum errors in dose calculation for different targets of four phantoms (with the extended calibration). Phantom 3 is not listed because of dose differences in Teflon cylinders.

	Ph. 1 (6 MV)		Ph. 2 (18 MeV)		Ph. 4 (18 MV)		Ph. 5 (18 MV)	
	Mean	Max	Mean	Max	Mean	Max	Mean	Max
Original CT image	4.6	13.6	4.3	51.2	3.1	10.6	4.6	43.4
Artifact corrected	0.7	1.9	0.4	1.5	0.6	3.0	3.1	6.9

deliberate dose calculation errors by incorrectly assigning the Teflon voxels to bone, so the material map for both the original CT and corrected geometry MC dose calculation is the exact material map taken from the exact geometry. Only the mass densities were assigned from the actual images according to the extended calibration. There is an improvement in the mean error of the target after artifact correction is done. The error decreases from 4.6% in the original CT image to 3.1% in the artifact-corrected image. Nevertheless, the inability of the calibration to retrieve the correct Teflon mass density prevents obtaining better results. This is also the reason why MC dose calculation results are not presented for phantom 3 that also exhibits large calculation errors in the Teflon cylinders.

Dose perturbation interface effects due to the presence of high-Z materials are an interesting issue that is usually neglected in commercially available dose algorithms. However, MC codes are able to simulate these effects caused by perturbations of secondary electron fluence.[35] The dose profile through the center of phantom 4 along the x direction is shown in Fig. 9. The 18 MV beam four field box dose profile clearly shows the dose perturbation at the water/metal interfaces at the position of the two steel cylinders.

C. Patient study

The metal artifact correction algorithm has been tested on several phantoms with a rather simple geometry. The advantage of this approach is that we can compare dose distributions of original and artifact-corrected images to dose calculations in the exact geometry. The metal streaking artifact correction algorithm has also been used on a hypothetical prostate patient and differences in dose volume histograms (DVHs) of a hypothetical target have been evaluated.

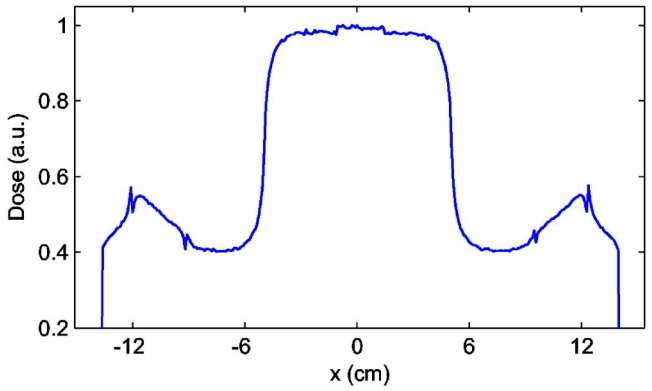

FIG. 9. Dose profile through the dose distribution of Fig. 8(a) (y=0 cm). Dose interface effects due to the presence of the steel cylinders are clearly visible (at x=−12, −9, 9, and 12 cm).

The patient study results are summarized in Figs. 10 and 11. The 18 MV photon beam dose distribution in the entire original CT image [Fig. 10(c)] is affected by streaking artifacts that are the most pronounced in the area between the hip prostheses [Fig. 10(a)]. The correction algorithm results in a more correct material segmentation and a smoother dose distribution in the artifact-corrected geometry [Fig. 10(d)]. We have also compared DVHs of an ellipsoidal target (outlined in Fig. 10) in order to quantify differences in the two dose distributions. Since the slice shown in Fig. 10 is almost at the edge of the target, the delineated circle appears small. An additional problem to the metal artifacts was found to arise. Due to incorrect assignment of some artifact influenced voxels to air in the original CT slice [Fig. 10(b)], about 20% of the target receives no dose [Fig. 11(a)]. It is common practice in MC dose calculations that the dose to air is set to zero, partly because the voxels filled with air have large calculation errors. Moreover, we are usually not interested in the dose outside the patient, or to air in body cavities. Figure 11(a) also shows that the entire target receives more than 80% of the maximum dose and the DVH curve is steeper in the artifact-corrected geometry. Figure 11(b) compares the dose distributions shown in Fig. 10 by plotting the differences between the dose in the original CT slice D_{CT} and the dose in the artifact-corrected slice D_{cor}. The two dose distributions were first normalized to the maximum dose in the artifact-corrected geometry and then subtracted. As expected, the negative dose differences appear in the voxels that have been incorrectly assigned to air in the original CT geometry, because the dose to these voxels is zero in the original geometry. The positive differences can be explained by incorrect assignment of some voxels to bone and subsequently larger energy deposition to bone than to tissue for the 18 MV photon beam. Our conclusion from the patient study is that the DVH curves for the original CT geometry and the corrected CT geometry differ significantly which is mostly due to the "zero dose to air" issue. Although the beam angles for our hypothetical MC simulation were taken from real prostate treatments as it is done in our hospital, it would be advisable to avoid the 90° and 270° beams. These should be replaced by beams that do not intersect the prostheses.

It has to be noted that metal artifact reduction techniques in general do not produce ideal artifact-free images. While the majority of the artifacts are reduced, some minor artifacts

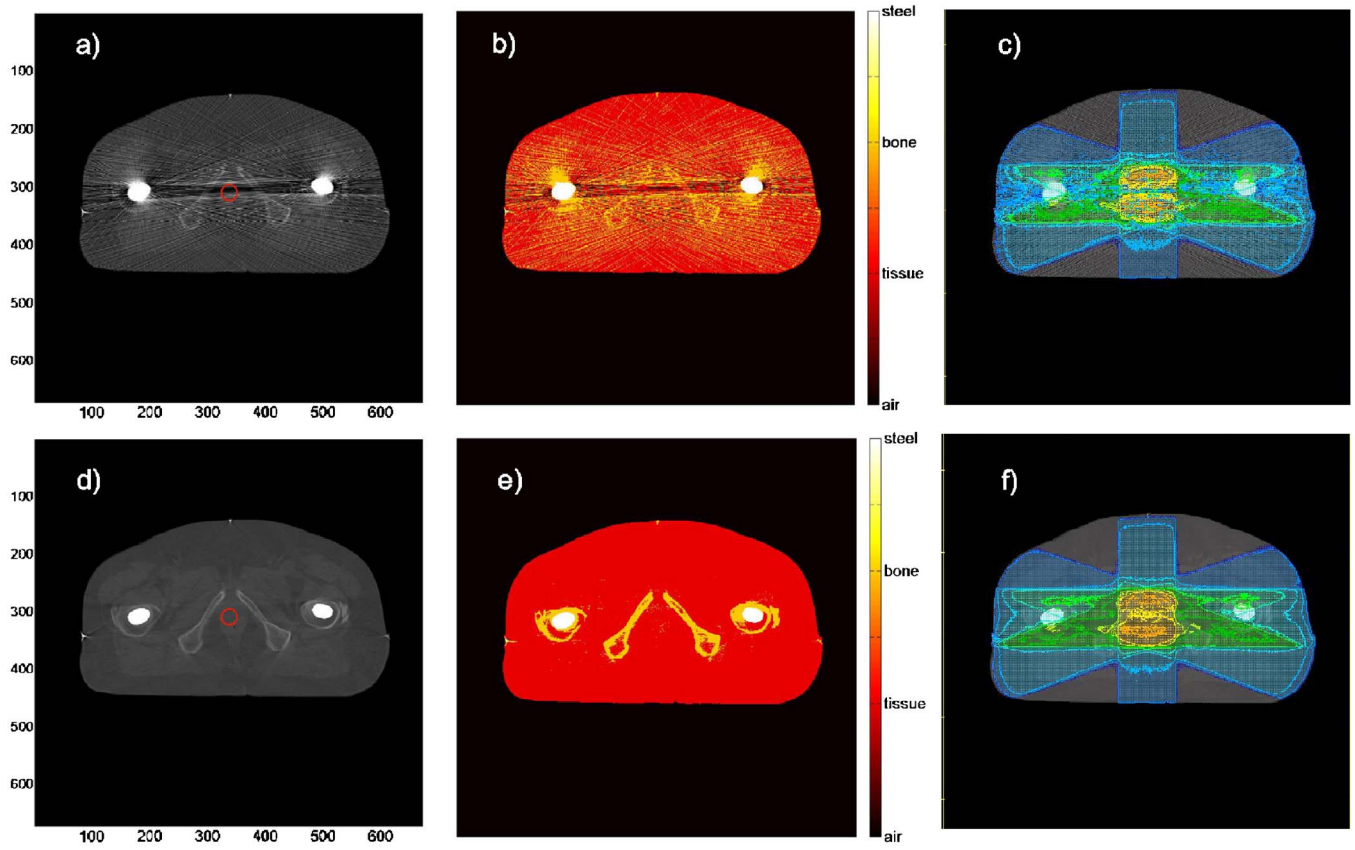

FIG. 10. Original CT image (a) and artifact-corrected image (d) of a prostate patient with an ellipsoidal target delineated. Material segmentation in the original CT image (b) and in the artifact-corrected image (e). Dose distribution in five-field 18 MV photon beam setup in the original CT image (c) and the artifact-corrected image (f).

are created, such as these around vial 7 in pelvic phantom 4 (Fig. 5). However, the net benefit for Monte Carlo dose calculations is demonstrated in this paper.

The Task Group 63 reported on dosimetric consideration for patients with hip prostheses undergoing pelvic irradiation.[13] First, they propose beam arrangements that partly or completely avoid hip prosthesis. Sometimes such an arrangement is not the best choice due to high dose to organs at risk and inhomogeneity correction for the prostheses is essential. In conventional treatment planning systems (TPS), the inhomogeneity correction can be calculated by the software by entering the correct electron densities for the pros-

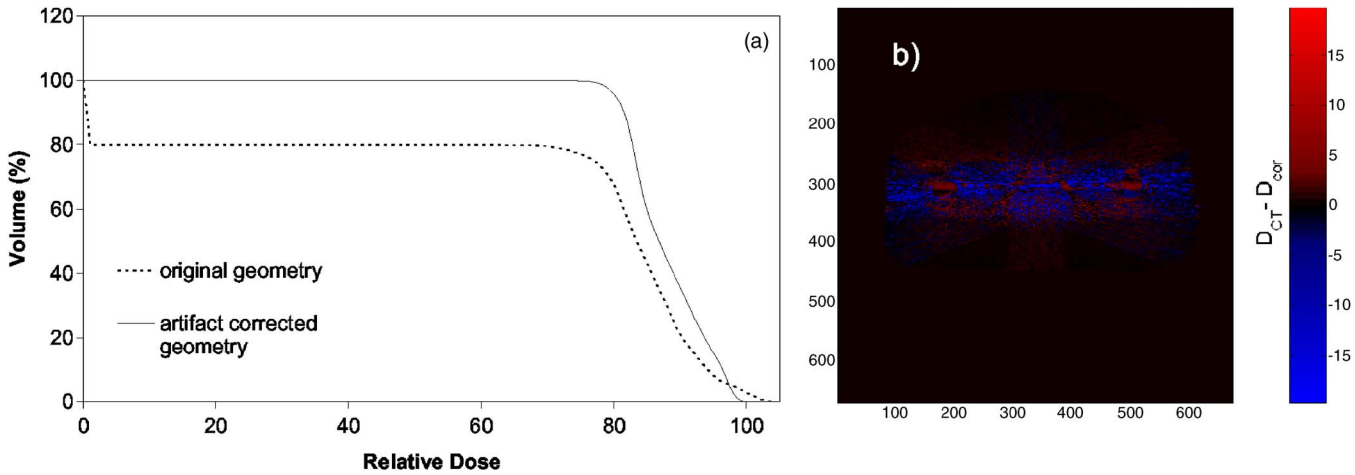

FIG. 11. DVHs for the target in the original CT geometry and in CT artifact-corrected geometry (a) and differences between the original CT geometry D_{CT} and the artifact-corrected geometry D_{cor} dose distributions $D_{CT}-D_{cor}$ (bright voxels have absolute differences larger or equal to 20%). The dose is normalized to the maximum dose in the artifact-corrected geometry in both images.

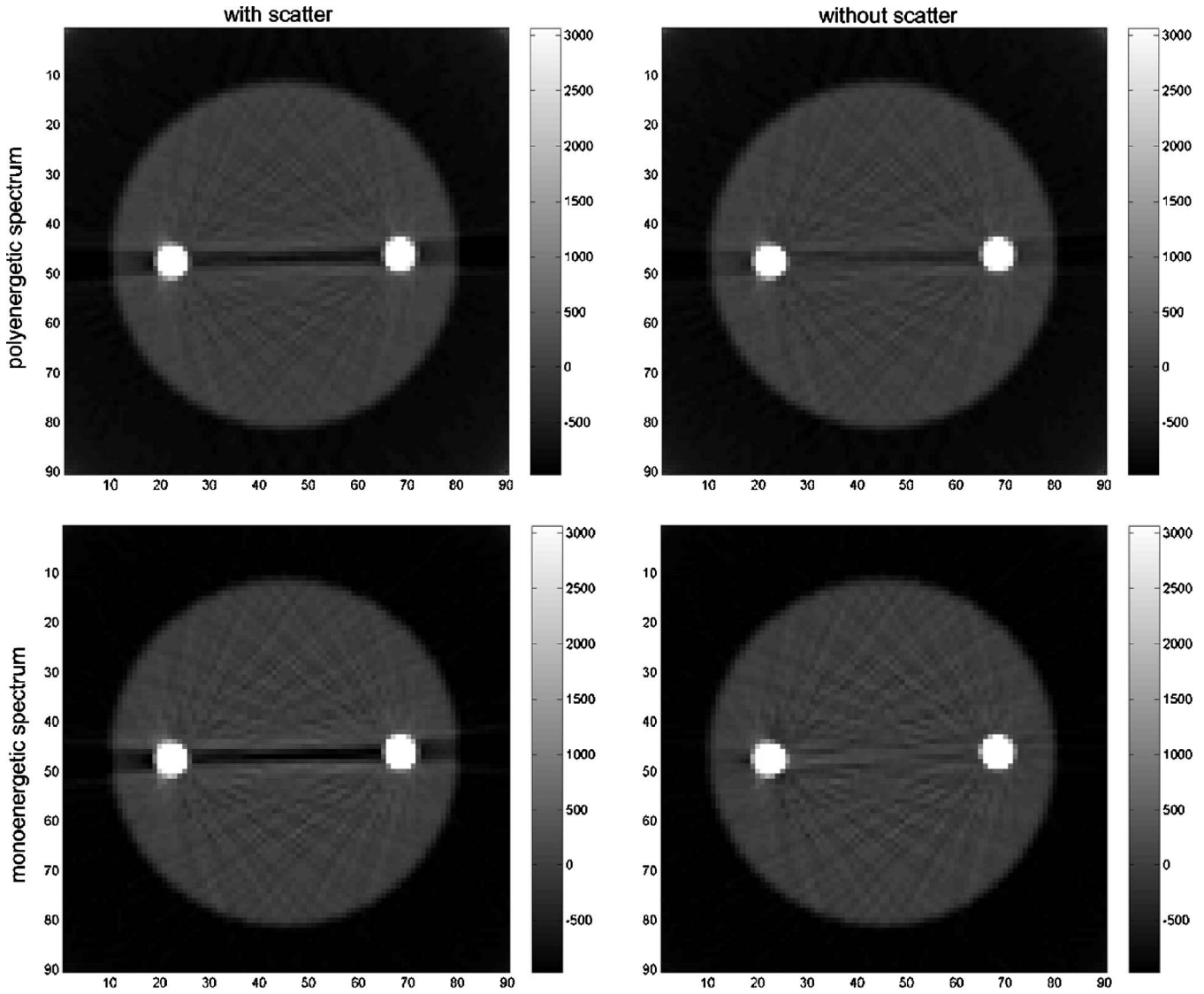

FIG. 12. CT image of the phantom simulated with a 120 kVp x-ray spectrum with scattered photons (a), with only primary photons (b); simulated with a monoenergetic 75 keV x-ray beam with scattered x rays (c), and with primary x rays only (d).

thesis material. The position and shape of the prosthesis has to be known. However, these are often very difficult to define in CT images containing artifacts. Metal artifact correction algorithms produce artifact reduced images and help identify the accurate position and shape of patients' prostheses. Finally, artifact corrected images can be used not only for MCTP but also for conventional TPS to properly account for tissue inhomogeneities.

D. Scatter and beam hardening as causes of metal streaking artifacts

The results from our preliminary study on scatter and beam hardening are summarized in Fig. 12. In order to quantify the differences in metal streaking artifacts, we present the mean HU of a rectangular water area extending between the steel cylinders. We will denote it as the test value. Without artifacts, the test value should correspond to HU of water (HU=0).

All the images contain subtle streaks that are produced by the small number of projections (360 projections over 360°) in our Monte Carlo simulation compared to real CT scanners that use on average ten times more projections. Nevertheless, the CT image obtained with the polyenergetic spectrum including scatter [Fig. 12(a)] is very similar to a real image produced by our CT scanner (not shown). The test value reads −80 HU which means that the density of this area is underestimated. The scatter-free image produced by the polyenergetic spectrum [Fig. 12(b)] shows less severe artifacts than the image with scatter. The HU in the area between the steel cylinders are higher, even though a dark streak is still visible. The test value for this case is −39 HU which is an improvement compared to −80 HU in Fig. 12(a). A monoenergetic spectrum was used to quantify the impact of beam hardening on metal streaking artifacts. As can be seen in Fig. 12(c), the artifacts are almost identical with the monoenergetic spectrum as with the polyenergetic spectrum

[Fig. 12(a)]. There is only a slight improvement in the test value which is −78 HU. On the other hand, Fig. 12(d) displays the scatter corrected image simulated with the monoenergetic spectrum that is almost artifact free. The test value improves significantly to 3 HU. We have to note that the contribution of scatter in our MC simulation is more significant than in real CT scanners. The real CT scanners accommodate an anti-scatter collimator that prevents some of the scattered photons from reaching the detectors and which was not modeled. On the other hand, the noise, which is another important source of metal streaking artifacts,[31] was not simulated at all. To summarize, whereas the scatter contribution is overestimated, the noise contribution is underestimated and Fig. 12(a) closely resembles the actual image obtained from the Picker scanner. Our results correspond to conclusions that Williamson *et al.*[31] drew in their paper.

Our study shows that in presence of scatter, the effect of beam hardening on metal streaking artifacts is minor. However, the best image is obtained with the primary monoenergetic beam. For the time being, it is not possible to use monoenergetic beams in CT scanners, however, a narrower spectrum can be obtained by adding appropriate filtration to the polychromatic x-ray beam. Also, the scatter contribution can be suppressed by using the smallest slice thickness. The collimators that define the slice thickness will help to avoid some of the scattered photons reaching the detectors.

IV. CONCLUSION

A method for correction of CT metal streaking artifacts was implemented and validated on several test phantoms and on a prostate patient. Impact of the artifact correction on MC dose calculation has been evaluated on both phantoms and the patient in a set of beam geometries. MC dose distributions have been calculated for original CT images and CT artifact-corrected images with the EGSnrc/DOSXYZnrc code. The phantom calculations were compared to dose calculation in the exact geometry; the patient's dose distributions were compared by DVHs of a hypothetical target.

The correction algorithm clearly allows to identify and delineate various structures that are invisible in images containing artifacts. We have found that in order to calculate dose accurately in between two metallic objects the artifact correction is essential. In addition, the procedure to convert HU values to a MC phantom has to be modified by adding an extra high-density material. In other words, an extended calibration has to be used. The errors in 6 MV photon dose calculations decreased from 25% for phantom images with CT artifacts when the default CT calibration was used to less than 2% for CT artifact-corrected images with the extended calibration. Similar improvement has been found for 18 MV photon beam and an 18 MeV electron beam dose calculations. A hypothetical treatment scenario of the prostate patient exhibits large differences in DVHs of a hypothetical target in the original geometry and in the artifact-corrected geometry, mainly due to miss-assignment of voxels to air in the presence of metal artifacts.

We have also briefly investigated scatter and beam hardening as causes of metal streaking artifacts. We have found that whereas beam hardening has a minor effect on metal artifacts, scattered photons are an important cause of these artifacts. A MC model of a CT scanner offers possibilities to reduce metal artifacts by removing scatter.

The metal streaking artifact correction algorithm results in a significant improvement in image quality, especially in the area between metallic objects, and makes material segmentation and dose calculation more accurate. Our work strongly demonstrates the need for a metal streaking artifact correction method in Monte Carlo treatment planning. Omission of a correction algorithm for streaking artifacts in MC planning systems will lead to large dose calculation errors and potential mistreatment of patients.

ACKNOWLEDGMENTS

The authors would like to acknowledge Dr. Catherine Coolens, Dr. John Roeske, and Dr. Jeffrey Williamson for helpful discussions, Dr. Fabio Cury for patient-related issues, Dr. Slobodan Devic for introduction to the CT scanner, Robin van Gils for phantom production, Dr. Mehran Yazdi for help with the correction algorithm, and Hatchig Ibisoglu from Philips for the Picker PQ5000 specifications. The work has been supported by Grant No. 206358 from the National Science and Engineering Research Council of Canada (NSERC). F.V. is a Research Scientist supported by the Fonds de Recherche en Santé du Québec (FRSQ).

[a]Electronic mail: fverhaegen@medphys.mcgill.ca

[1]C.-M. Ma, E. Mok, A. Kapur, T. Pawlicki, D. Findley, S. Brain, K. Forster, and A. L. Boyer, "Clinical implementation of a Monte Carlo treatment planning system," Med. Phys. **26**, 2133–2143 (1999).

[2]J. Hsieh, "Image artifacts, causes, and corrections," in *Medical CT and Ultrasound: Current Technology and Applications*, edited by L. W. Goldman and J. B. Fowlkes (Advanced Medical, Madison, WI, 1995), pp. 487–518.

[3]T. Pawlicki and C. M. Ma, "Effect of CT streaking artifacts in Monte Carlo dose distributions for head and neck cancer," *XIII. International Conference on the Use of Computers in Radiation Therapy 2000*, Heidelberg Germany, 414–416.

[4]W. A. Kalender, R. Hebel, and J. Ebersberger, "Reduction of CT artifacts caused by metallic implants," Radiology **164**, 576–577 (1987).

[5]J. C. Roeske, C. Lund, C. A. Pelizzari, X. Pan, and A. J. Mundt, "Reduction of computed tomography metal artifacts due to the Fletcher-Suit applicator in gynecology patients receiving intracavitary brachytherapy," Brachytherapy **2**, 207–214 (2003).

[6]M. Yazdi, L. Gingras, and L. Beaulieu, "An adaptive approach to metal artifact reduction in helical computed tomography for radiation therapy treatment planning: Experimental and clinical studies," Int. J. Radiat. Oncol., Biol., Phys. **62**, 1224–1231 (2005).

[7]J. Hsieh, "Adaptive streak artifact reduction in computed tomography resulting from excessive x-ray photon noise," Med. Phys. **25**, 2139–2147 (1998).

[8]D. L. Snyder, T. J. Schultz, and J. A. O'Sullivan, "Deblurring subject to non-negativity constraints," IEEE Trans. Signal Process. **40**, 1143–1150 (1992).

[9]G. Wang, D. L. Snyder, J. A. O'Sullivan, and M. W. Vannier, "Iterative deblurring for CT metal artifact reduction," IEEE Trans. Med. Imaging **15**, 657–664 (1996).

[10]P. J. Keall, L. B. Chock, R. Jeraj, J. V. Siebers, and R. Mohan, "Image reconstruction and the effect on dose calculation for hip prostheses," Med. Dosim. **28**, 113–117 (2003).

[11]D. Xia, J. C. Roeske, L. Yu, C. A. Pelizzari, A. J. Mundt, and X. Pan, "A hybrid approach to reducing computed tomography metal artifacts in in-

tracavitary brachytherapy," Brachytherapy **4**, 18–23 (2005).
[12]B. De Man, J. Nuyts, P. Dupont, G. Marchal, and P. Suetens, "An iterative maximum-likelihood polychromatic algorithm for CT," Med. Phys. **20**, 999–1008 (2001).
[13]C. Reft, R. Alecu, I. J. Das, B. J. Gerbi, P. Keall, E. Lief, B. J. Mijnheer, N. Papanikolaou, C. Sibata, and J. Van Dyk, AAPM Radiation Therapy Committee Task Group 63, "Dosimetric considerations for patients with HIP prostheses undergoing pelvic irradiation. Report of the AAPM Radiation Therapy Committee Task Group 63," Med. Phys. **31**, 1162–1182 (2003).
[14]X. Pan, "Optimal noise control in and fast reconstruction of fan-beam computed tomography image," Med. Phys. **26**, 689–697 (1999).
[15]B. R. B. Walters and D. W. O. Rogers, "DOSXYZNRC Users Manual," NRCC Report No. PIRS 794 (2002).
[16]J. Seco, E. Adams, M. Bidmead, M. Partridge, and F. Verhaegen, "Head-and-neck IMRT treatments assessed with a Monte Carlo dose calculation engine," Phys. Med. Biol. **50**, 817–830 (2005).
[17]X. A. Li, L. Ma, S. Naqvi, R. Shih, and C. Yu, "Monte Carlo dose verification for intensity-modulated arc therapy," Phys. Med. Biol. **46**, 2269–2282 (2001).
[18]S. Stapleton, S. Zavgorodni, I. A. Popescu, and W. A. Beckham, "Implementation of random set-up errors in Monte Carlo calculated dynamic IMRT treatment plans," Phys. Med. Biol. **50**, 429–439.
[19]C. Boudreau, E. Heath, J. Seutjens, O. Ballivy, and W. Parker, "IMRT head and neck treatment planning with a commercially available Monte Carlo based planning system," Phys. Med. Biol. **50**, 879–890 (2005).
[20]A. Leal, F. Sanchez-Doblado, R. Arrans, J. Rosello, E. C. Pavon, and J. I. Lagares, "Routine IMRT verification by means of an automated Monte Carlo simulation system," Int. J. Radiat. Oncol., Biol., Phys. **56**, 58–68 (2003).
[21]T. Pawlicki and C.-M. Ma, "Monte Carlo simulation for MLC-based intensity-modulated radiotherapy," Med. Dosim. **26**, 157–168 (2001).
[22]P. Francescon, S. Cora, and P. Chiovati, "Dose verification of and IMRT treatment planning system with the BEAM EGS4-based Monte Carlo code," Med. Phys. **30**, 144–157 (2003).
[23]E. D. Yorke, L. Wang, K. E. Rosenzweig, D. Mah, J. B. Paoli, and C. S. Chui, "Evaluation of deep inspiration breath-hold lung treatment plans with Monte Carlo dose calculation," Int. J. Radiat. Oncol., Biol., Phys. **53**, 1058–1070 (2002).
[24]L. Wang, E. Yorke, and C. S. Chui, "Monte Carlo evaluation of tissue inhomogeneity effects in the treatment of the head and neck," Int. J. Radiat. Oncol., Biol., Phys. **50**, 1339–1349 (2001).
[25]F. C. Du Plessis, C. A. Willemse, M. G. Lotter, amd L. Goedhals, "Comparison of the Batho, ETAR and Monte Carlo dose calculation methods in CT based patient models," Med. Phys. **28**, 582–589 (2001).
[26]W. Schneider, T. Bortfeld, and W. Schlegel, "Correlation between CT numbers and tissue parameters needed for Monte Carlo simulations of clinical dose distributions," Phys. Med. Biol. **45**, 459–478 (2000).
[27]C. Coolens and P. J. Childs, "Calibration of CT Hounsfield units for radiotherapy treatment planning of patients with metallic hip prostheses: The use of extended CT scale," Phys. Med. Biol. **48**, 1591–1603 (2003).
[28]R. Mohan, C. Chui, and L. Lidofsky, "Energy and angular distributions of photons from medical linear accelerators," Med. Phys. **12**, 592–597 (1985).
[29]A. F. Bielajew, "Fundamentals of the Monte Carlo method for neutral and charged particle transport," Course notes, University of Michigan (2001).
[30]B. De Man, J. Nuyts, P. Dupont, G. Marchal, and P. Suetens, "Metal streak artifacts in x-ray computed tomography: A simulation study," IEEE Trans. Nucl. Sci. **46**, 691–696 (1999).
[31]J. F. Williamson, B. R. Whiting, J. Benac, R. J. Murphy, G. J. Blaine, J. A. O'Sullivan, D. G. Politte, and D. L. Snyder, "Prospects for quantitative computed tomography imaging in the presence of foreign metal bodies using statistical image reconstruction," Med. Phys. **29**, 2404–2418 (2002).
[32]D. W. O. Rogers, B. A. Faddegon, G. X. Ding, C.-M. Ma, and J. We, "BEAM: A Monte Carlo code to simulate radiotherapy treatment units," Med. Phys. **22**, 503–524 (1995).
[33]D. L. Parker, "Optimal short scan convolution reconstruction for fan-beam CT," Med. Phys. **9**, 254–257 (1982).
[34]F. Verhaegen and S. Devic, "Sensitivity study for CT image use in Monte Carlo treatment planning," Phys. Med. Biol. **50**, 937–946 (2005).
[35]F. Verhaegen and I. Das, "Interface dosimetry for kV and MV photon beams," in *Recent Developments in Accurate Radiation Dosimetry* edited by J. Seuntjens and P. Mobit (Medical Physics, Madison, WI, 2002).